Available online at www.sciencedirect.com
SCIENCE DIRECT®
Physics of the Earth and Planetary Interiors 148 (2005) 39–54
PHYSICS OF THE EARTH AND PLANETARY INTERIORS
www.elsevier.com/locate/pepi

Mantle structure from inter-station Rayleigh wave dispersion and its tectonic implication in western China and neighboring regions

Huajian Yao, Guoming Xu*, Liangbao Zhu, Xiang Xiao

Department of Earth and Space Sciences, University of Science and Technology of China, Hefei, 230026 Anhui, PR China

Received 16 December 2003; received in revised form 27 July 2004; accepted 4 August 2004

Abstract

We processed more than 3000 inter-station great circle paths to determine the phase velocity for the fundamental mode of Rayleigh wave, and finally arrived at 110 paths of high quality dispersion data, which show good spatial coverage in western China and neighboring regions. Rayleigh wave phase velocity dispersion model WChina1D was obtained and compared with previous global and regional models. Phase velocity maps from 15 to 120 s were inverted and the maps of 20, 40, 80, and 120 s are presented in this paper. Checkerboard tests show the average lateral resolution in our area of interest is about 7°. Our tomographic results corroborate a prominent low-velocity anomaly lying mainly in the lower crust and uppermost mantle in the Chang Thang terrane. The apparent low-velocity anomaly also appears in the wide area of northeastern Tibet in the crust and upper mantle. The low-velocity area around southeastern Tibet may be created by the southeastern migration of the low-velocity mass of the Tibetan plateau. The eastern Tarim shows structure with higher velocities relative to that of central Tarim. A large-scale low-velocity anomaly is clearly seen in central and western Mongolia. Our high quality measurements were also used to evaluate the CUB global shear velocity model [Shapiro, N., Ritzwoller, M., 2002. Monte-Carlo inversion for a global shear-velocity model of the crust and upper mantle. Geophys. J. Int. 151, 88–105] of the crust and upper mantle. The 40 s Rayleigh phase velocity map predicted from CUB model shows an apparent discrepancy with our measurements in western China and western Mongolia, which implies a higher estimated (about +1–2%) phase velocity model in these regions, probably due to the Gaussian smoothing condition in their tomography inversion.

Keywords: Western China and neighboring regions; Rayleigh wave; Phase velocity; Inter-station

1. Introduction

The region of western China and neighboring area has long been the focus of geophysical studies for its complex topography and tectonic structure (Fig. 1). It is widely known that the Indian plate collided to the northward with the Asian plate from around 40–50 Ma (Molnar and Tapponnier, 1978), to form the Tibet–Pamir plateau, the highest in the world. The Tarim basin, separated from the Tibetan plateau by the Kunlun fold system, consists of a nucleus of Archean through Proterozoic age covered by thick Cenozoic sediments. The Tarim basin and the Sino-Korean plat-

* Corresponding author.
E-mail address: xugm@ustc.edu.cn (G. Xu).

0031-9201/$ – see front matter © 2004 Elsevier B.V. All rights reserved.
doi:10.1016/j.pepi.2004.08.006

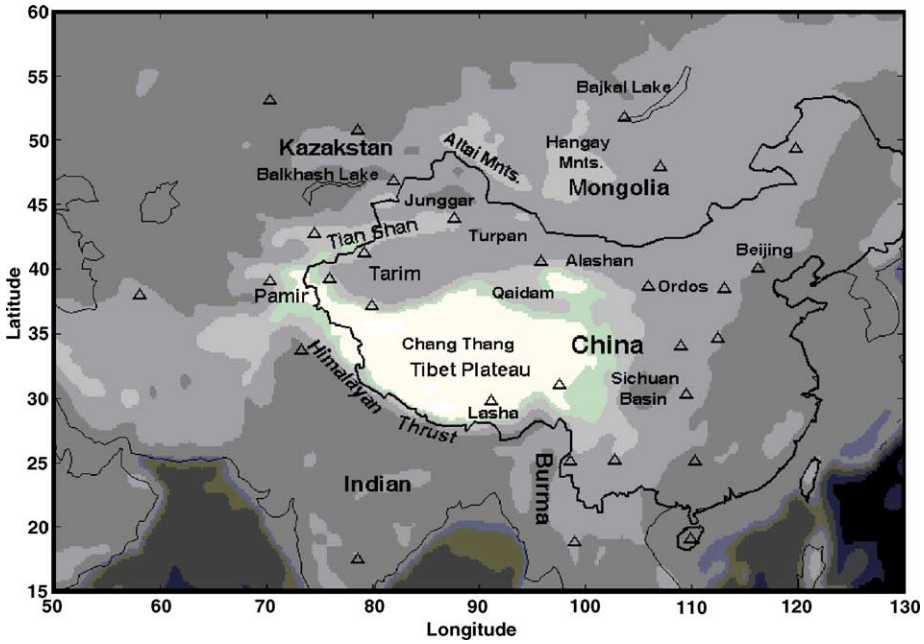

Fig. 1. Locations of the used stations and geological sketch map of the China and adjacent regions. The symbol △ indicates the location of stations.

form collided with the Siberian craton in the early Paleozoic, creating a series of west–east mountain chains: the Tianshan in Kyrgyzstan and western China, the Beishan near the Mongolian border and the Yinshan in the Inner Mongolia of China. South of the Tibetan plateau, the Yangtze platform was consolidated and stabilized after the Yangtze orogeny (ca. 825 Ma) and was separated from the Sino-Korean platform by the Qinling fold system in the early Mesozoic.

In the past two decades, seismologists have performed numerous studies using body and surface waves to investigate the velocity structure of the crust and upper mantle. For the surface wave approach, the traditional dispersion method (Brune et al., 1960; Bloch and Hales, 1968; Dziewonski et al., 1969; Landisman et al., 1969) and recent waveform inversion methods (Cara and Leveque, 1987; Nolet, 1990; Trampert and Woodhouse, 1995; Yoshizawa and Kennett, 2002a, 2002b) have been widely adopted for the global and regional tomographic studies. In regional and global surface wave tomography, most studies were based on ray theory and great circle approximation, for instance, Trampert and Woodhouse (1995), Curtis et al. (1998), Ritzwoller and Levshin (1998). Ray theory, however, is only valid if the scale length of heterogeneity is larger than the wavelength and the width of the first Fresnel zone. Nowadays, scattering theories and its application in the estimation of surface wave maps or Earth models are becoming increasingly common in the literature (Ritzwoller et al., 2002; Spetzler et al., 2002; Yoshizawa and Kennett, 2002a, 2002b) in order to obtain more accurate and high-resolution regional or global S-velocity models. In the region of Central Asia and China, there are surface wave group velocity tomography studies using single-station dispersion method by Feng and Teng (1983), Jobert et al. (1985), Wu and Levshin (1994), Ritzwoller and Levshin (1998), Ritzwoller et al. (1998), Zhu et al. (2002), Huang et al. (2003); phase velocity dispersion studies using the inter-event method by Romanowicz (1982), Brandon and Romanowicz (1986), Bourjot and Romanowicz (1992) and Curtis and Woodhouse (1997); phase velocity tomography studies using single-station waveform inversion method by Curtis et al. (1998) and Griot and Montagner (1998). For this region, the surface wave tomography studies mentioned above were all based on ray theory.

In all single-station measurements of group velocity dispersion, the main errors, generally regarded as 'theoretical errors', are from the following five sources: (1) off great-circle effect, (2) azimuthal anisotropy effect in surface wave propagation, (3) mislocations of earthquake epicenters, (4) source origin time errors and (5) the finite dimension and duration of source process. Here, we refer to the errors from the first two sources as 'structure term errors', which are caused by the propagation of seismic waves in complex structure and the errors from the last three sources as 'source term errors' which are caused by source problems. In the measurements of phase velocities with inter-event or single-station waveform inversion methods, the Harvard CMT (centroid moment tensor) parameters are necessary for the determination of the initial phase delay time. Besides 'structure term errors', inter-event and single-station waveform inversion methods of phase velocity measurements also introduce errors from source, especially from the mislocations of earthquake epicenters. Compared with group velocity measurements, phase velocity measurements from waveform inversion method are much more complicated because of high non-linearity and great attention must be taken to resolve the 2π phase ambiguity at short periods (Trampert and Woodhouse, 2001). In most studies using inter-event method (Romanowicz, 1982; Brandon and Romanowicz, 1986; Curtis and Woodhouse, 1997), only mixed path phase velocity dispersion was obtained because of the lack of sufficient path coverage, except for the study by Bourjot and Romanowicz (1992). Besides the methods discussed above, the inter-station method is the most accurate method in the determination of surface wave velocity (great circle phase velocity) by using the phase difference of two multiple phases (Sato, 1958) because it can almost completely remove 'source term errors'. But inter-station method also has its disadvantage from the lack of sufficient stations located in the region of study, which causes the sparse path coverage. So most previous phase velocity studies using the inter-station method (Feng et al., 1983; Calcagnile, 1991; Snoke and James, 1997; Brisbourne and Stuart, 1998) have only obtained mixed phase velocity dispersion along the great circle paths linking two stations and thereby only the average velocity structure was inverted along each inter-station path. Xu et al. (2000) made an attempt to construct Rayleigh wave phase velocity maps with inter-station dispersion measurements and invert the 3D *SV* structure in the crust and upper mantle of east continental China. But only 43 paths were used in their study, which could not provide a good lateral resolution for the region of interest.

In the past decade, more and more high quality broadband seismic stations from both global seismic network (e.g., GDSN, GSN, Geoscope) and regional seismic network (e.g., CDSN, KNET, KAZNET) have been installed in the Central and East Asia. A set of newly installed broadband stations in China has greatly improved the station density in our studied region. Both the station number and data quality provide us more accurate dispersion data than before by using inter-station method.

In this paper, we firstly used the inter-station method to obtain high quality phase velocity of Rayleigh wave fundamental mode for 110 paths, which form a good spatial and azimuthal path coverage in the studied region. We implemented a GUI software based on image analysis technique to implement the quick determination of the phase velocity dispersion curve using narrow band filtering and cross-correlation method. With the help of this software more than 3000 inter-station paths (include many multiple paths which link the same two stations) were analyzed accurately. After careful examination, only the 110 highest quality dispersion data from period 15–120 s were chosen for the next inversion step. An average 1D Rayleigh wave phase velocity model in western China and adjacent regions, called WChina1D, was derived and compared with the models in previous studies. The Gaussian tomography method (Tarantola and Nercessian, 1984) based on ray theory was applied to construct Rayleigh wave phase velocity maps from 15 to 120 with the period interval of 5 s. Checkerboard tests show the average lateral geometrical resolution across the studied region is about 7°. Some inversion results of the 1D dispersion data for some critical points in our studied regions were shown and further explained. We also used our high quality measurements to evaluate the latest CUB global shear velocity model of the crust and upper mantle (Shapiro and Ritzwoller, 2002) for the studied regions.

2. Data and measurement

We used the inter-station method to determine the phase velocity of Rayleigh wave fundamental mode

in the period range 15–120 s, with the assumption that the surface waves propagate along the great circle path. Fig. 1 shows the locations of the broadband stations from different seismic networks, including global seismic networks (e.g., GDSN, GSN, Geoscope) and regional seismic networks (e.g., CDSN, KNET, KAZNET). The earthquakes used in this study are all have magnitude $5.0 < \mathrm{Mw} < 6.8$ and depth less than 100 km. The epicentral distances are all in the range 20–130°, in order to avoid near-source effects and interference from higher modes of Rayleigh wave. Because only Rayleigh wave phase velocity was picked here, we only selected vertical component waveforms. Most of the records we used were from IRIS (Incorporated Research Institutes for Seismology) data center and the other records were from the data center of CDSN. Only waveforms that were clear at both stations with the angle between the earthquake and inter-station paths less than 2° are used here. Knopoff et al. (1966) showed that the errors in azimuth arising from refraction would introduce only second order effects in phase velocity provided that the angle between the earthquake and inter-station paths is small.

The measurement of phase velocities was based on the cross-correlation method (Bloch and Hales, 1968). We designed a Matlab GUI software based on an image analysis technique (Yao et al., 2004) to implement the determination of the phase velocity dispersion curve. First, the instrument responses were removed from both inter-station records with clear Rayleigh wave trains. Then, the MFT (multiple filter technique) method (Dziewonski et al., 1969) was used to determine the group arrival times of Rayleigh wave fundamental mode. We only chose the inter-station records with both clear and continuous Rayleigh wave fundamental mode on the period-group velocity energy diagram. Before narrow band filtering of the two records, a time window $w(t, T_c)$ with cosine shoulder (Eq. (1)) was used to window the seismograms and each window was centered at the group arrival time of fundamental mode corresponding to the period of interest:

$$w(t, T_c) = \begin{cases} 1, & t_g(T_c) - nT_c < t < t_g(T_c) + nT_c \\ \cos\left(\pi \dfrac{|t - t_g(T_c)| - nT_c}{T_c}\right), & -\dfrac{T_c}{2} < |t - t_g(T_c)| - nT_c < \dfrac{T_c}{2} \\ 0, & \text{elsewhere} \end{cases} \quad (1)$$

Here, T_c is the period of interest and $t_g(T_c)$ is the group arrival time at period T_c. n is a window constant with typical value 2–3, which denotes that half window length is about n times of each interested period. This window was designed to eliminate noise of higher mode waves and other waves we are not interested in our studies, and was quite successful in practical applications. The windowed seismograms of both stations were filtered with a narrow band pass filter, a windowed linear-phase FIR band pass digital filter with the band of 0.4 s at each period of interest. A Kaiser window for the FIR filter was finally selected for the quality of filtering after careful comparisons with Hamming, Hann, Blackman, Bartlett and Chebwin windows. The period range used is 15–120 s with a period interval of 1 s. The cross-correlation amplitude image was obtained for each inter-station pair after cross-correlation of the two filtered seismograms. Because the cross-correlation amplitude image is indirect in the relationship between the periods and phase velocities, we use 3-spline interpolation to transform the cross-correlation amplitude image (commonly part of this image) to a phase velocity image (Fig. 2). It is very convenient to implement this transformation by using the image analysis technique of our GUI software. On the phase velocity image the required dispersion curve was automatically picked (Fig. 2) with high accuracy by the quick tracing scheme developed in our software. Because the entire process of data processing was interactive and the interface was graphical, it gave us a convenient and objective judgment of the quality of dispersion data.

More than 3000 inter-station paths (including multiple paths) from the years 1990 to 2001 were processed. After careful examination and comparison, the dispersion data for 110 paths with the best quality and reliability were finally used to invert for the phase velocity maps. Fig. 3 shows the distribution of the inter-station paths. The spatial coverage of paths was relatively good in our studied regions except in the Indian shield and in the western Pamir. The average error of phase velocity

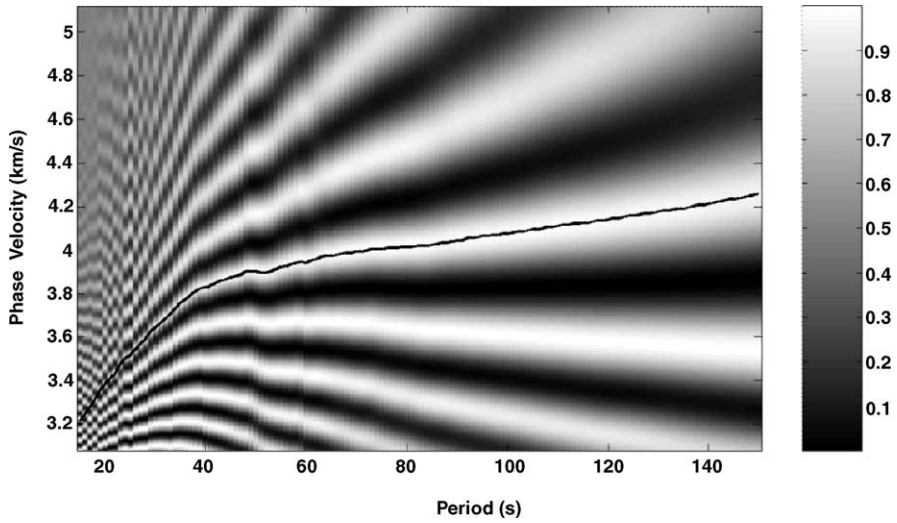

Fig. 2. Example of phase velocities determination of inter-station paths based on image analysis technique. The solid line in the image is the phase velocity dispersion curve automatically traced by our GUI software. The period range is from 15 to 150 s in this example. Two stations are BJT and WUS. Date, 25 October 1999, 07:29:55.5900; location, 31.971°N, 142.251°E, 33.0 km; magnitude, Mw = 5.8.

varies with period. The phase velocity errors at period higher than 35 s were not larger than 0.04 km/s (about 1%), which is mainly arises from small angle deviations between the earthquake and inter-station paths. The errors at period below 30 s may be up to 0.05–0.08 km/s (about 1.5–2.5%) because of the possible indeterminate 2π phase ambiguity in the phase velocity image at shorter periods. But for most of the inter-station paths we finally used, the phase velocity measurements are quite good even for periods lower than 30 s.

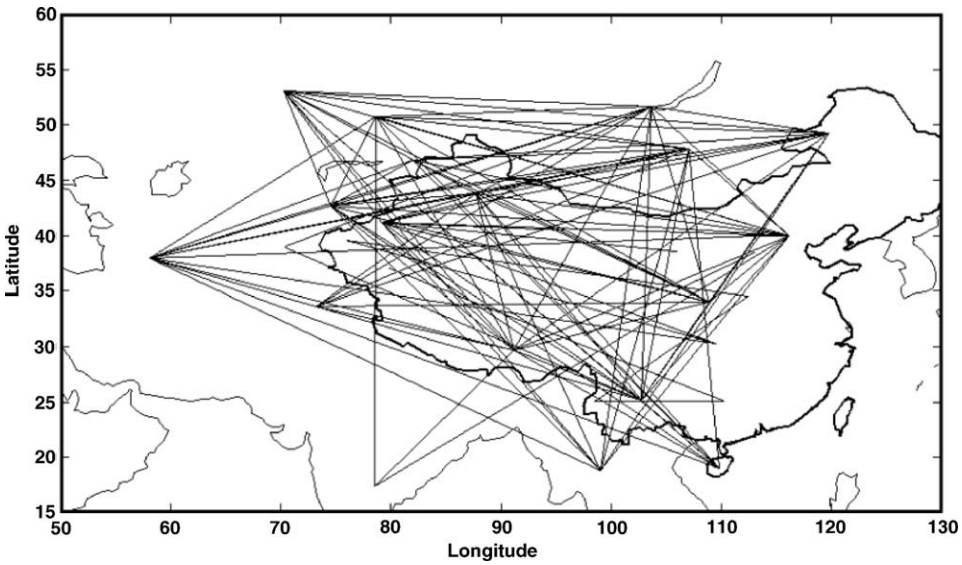

Fig. 3. Path coverage in our study (total 110 inter-station paths of Rayleigh wave).

We constructed a one-dimensional phase velocity dispersion model for our studied area by taking the average value of all measured 110 phase velocity dispersion data. The average group velocity model was computed by:

$$u(T) = \frac{c(T)}{1 + (T/c(T))(\mathrm{d}c(T)/\mathrm{d}T)} \quad (2)$$

Here, $u(T)$ is the group velocity and $c(T)$ is the phase velocity.

Here, we call this model as WChina1D (Fig. 4). In Fig. 4a, we also show Rayleigh wave phase velocity dispersion model Eurasia1D (Curtis et al., 1998) and the results from PEMc (Dziewonski et al., 1975) and PREM (Dziewonski and Anderson, 1981). The phase velocities at all periods of WChina1D are lower than those of PREM, PEMc and Eurasia1D. In the study of Curtis et al. (1998), the average crust thickness of their studied area is about 40 km, but in our studied area the average crust thickness is 50 km or more. At periods lower than 45 s the Rayleigh wave phase velocities of WChina1D are about 0.2 km/s less than that of Eurasia1D, but at higher periods (>70 s) the difference of the phase velocities between the two models is about less than 0.05 km/s. The main reason for the difference between Eurasia1D and WChina1D is the different average crust thickness in the studied area. Fig. 4b gives the comparisons of group velocity of WChina1D with Eurasia1D (Curtis et al., 1998) and the average group velocity (RitzLev97) obtained by Ritzwoller and Levshin (1998). Similar to the results of phase velocities, at periods below 65 s, the group velocity of WChina1D is significantly less than that of RitzLev97 and Eurasia1D, but the difference of group velocities decreases to less than 0.1 km/s at periods above 75 s. Because the inter-station paths we used here are well confined and distributed in this area, our model WChina1D could well represent the dispersion feature of Rayleigh wave fundamental mode in western China and the neighboring regions.

3. Tomographic method and resolution

The Gaussian tomography method (Tarantola and Nercessian, 1984) based on ray theory was used to invert the phase velocity map in our studied regions by minimizing the cost function:

$$\Phi(m) = (d_0 - d)^{\mathrm{T}} C_{d_0}^{-1} (d_0 - d) + (m_0 - m)^{\mathrm{T}} C_{m_0}^{-1} (m_0 - m) \quad (3)$$

Here, d_0 is a vector of observed arrival time data in a fixed period, d is a vector of arrival time predicted from the actual slowness model m through an equation of the form $d = g(m)$, m_0 is an a priori slowness model, C_{d_0} is the data covariance matrix describing the data uncertainties and C_{m_0} is an a priori covariance function describing our confidence in the a priori model m_0.

The solution of Eq. (3) could be obtained by:

$$m_{k+1}(r) = m_0(r) + \sum_i W_k^i \int_{R^i(m_k)} \mathrm{d}s^i \, C_{m_0}(r, r^i) \quad (4a)$$

$$W_k^i = \sum_j (S_k^{-1})^{ij} V_k^j \quad (4b)$$

$$S_k^{ij} = (C_{d_0})^{ij} + \int_{R^i(m_k)} \mathrm{d}s^i \int_{R^j(m_k)} \mathrm{d}s^i \, C_{m_0}(r, r^i) \quad (4c)$$

$$V_k^j = d_0^j - \int_{R^j(m_k)} \mathrm{d}s^j \, m_0(r^j) \quad (4d)$$

Here, i and j are path index and the integral path $R^i(m_k)$ is along the ith great circle path. It is assumed that the measurements of phase velocity are independent for each path. In this case, C_{d_0} is a diagonal matrix and the diagonal terms σ_d^i represent the square of the estimated error in our measurement of Rayleigh wave arrival time for path i. The origin of the actual errors in the measurements of phase velocity has many aspects, including 'structure term errors', the error caused by the small angle between the earthquake and inter-station paths and the error from the indeterminate 2π phase ambiguity in the phase velocity image at shorter periods. As discussed in Section 2, we estimate the average error $\varepsilon(T)$ (in percentage) in phase velocity measurements at each period T: $\varepsilon(T)$ was set to be 2.5% at 15 s, 2% at 20 s and 25 s, 1.5% at 30 s and 1% at period 35–120 s. So the corresponding error σ_d^i could be easily calculated at different periods along each path by the term $\sigma_d^i = \varepsilon(T)\Delta^i / c^i(T)$ in which $c^i(T)$ is the phase velocity at period T and Δ^i is the inter-station great circle distance of path i.

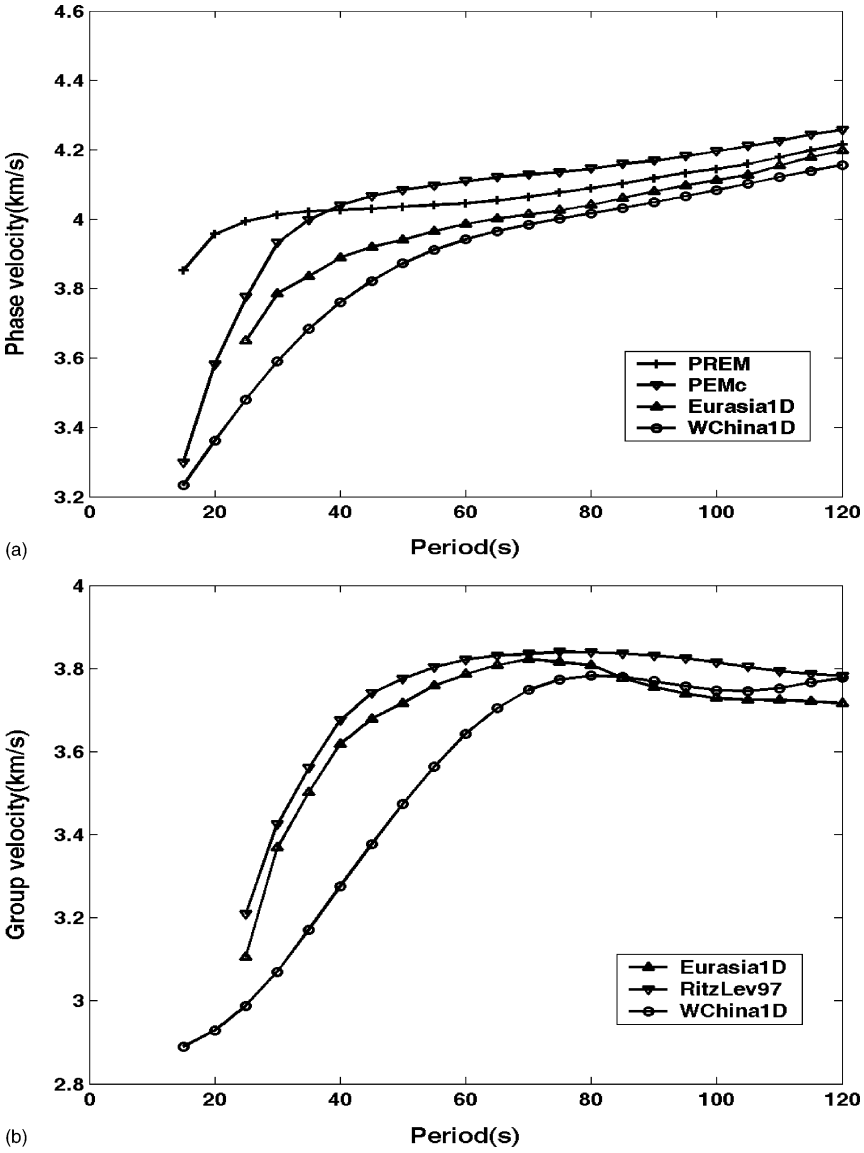

Fig. 4. One-dimensional Rayleigh wave velocity model WChina1D. (a) Phase velocities and comparison with the results of pervious models. (b) Group velocities and comparison with previous results.

The a priori covariance function $C_{m_0}(r, r')$ represents the covariance between points r and r' with the analytical form of:

$$C_{m_0}(r, r') = \sigma_m^2 \exp\left[-\frac{0.5(r - r')^2}{L^2}\right] \quad (5)$$

where σ_m represents the a priori slowness uncertainty at each point and L represents the correlation length of uncertainties. In our studies it is more convenient to estimate the a priori phase velocity uncertainty σ_p and then convert σ_p to the a priori slowness uncertainty σ_m. The starting phase velocity or slowness model for each period is an average model in which the value at each grid point is taken directly from our WChina1D

results. After many tests, σ_p was finally set at the value of 0.3 km/s, so the corresponding value of σ_m approximates 0.02 s/km. The correlation length L is mainly dependent on the spatial and azimuthal coverage of paths and the wavelength of wave compared to the scale of heterogeneities. A popular method to determine the value of L is through the checkerboard tests although this method also has essential weakness (Lévêque et al., 1993). The main function of checkerboard tests is to estimate the spatial and azimuthal resolution of different studied regions. First we divided the studied geographic area into grids of $1^\circ \times 1^\circ$. Then we performed checkerboard tests with different correlation length and geographic block. Here, we finally chose 450 km as the value of correlation length L with which we could well resolve lateral heterogeneity about 7° in our area of interest (Fig. 5).

4. Rayleigh phase velocity maps

From the tomographic method discussed in Section 3, we constructed phase velocity maps of Rayleigh wave for the period range from 15 to 120 s with the period interval of 5 s. The initial model was the average slowness model directly from our Rayleigh wave WChina1D model. Fig. 6 shows the tomographic results for periods 20, 40, 80, and 120 s.

At 20 s, the phase velocities are much influenced by the shallow and middle part of the crust. On this map (Fig. 6a), the Tibetan plateau, the Tarim basin, part of Tianshan and the Junggar basin show low-velocity anomalies, while a large high-velocity anomaly lies in the region of South China block and the region around Balkhash Lake. The most conspicuous low-velocity anomaly (−6–10%) appears in eastern Tibet, that appears to differ from the 26 s Rayleigh wave phase velocity map of Curtis et al. (1998). At 40 s, the phase velocities are strongly influenced by the crust thickness in our studied area. On this map (Fig. 6b) the most dominant feature is the east–west direction low-velocity anomaly lying in the Tibetan plateau mainly due to its very thick crust. This feature is similar to many previous group and phase velocity tomography studies (Ritzwoller and Levshin, 1998; Zhu et al., 2002; Huang et al., 2003; Curtis et al., 1998; Trampert and Woodhouse, 1995, 1996; Ekstrom et al., 1997). The magnitude of this low-anomaly on our 40 s map appears to be larger than that of the global phase velocity studies by Trampert and Woodhouse (1995, 1996) and is also larger than in the regional 40 s phase velocity map by Curtis et al. (1998) especially in eastern and northeastern Tibet. A low-velocity anomaly (−2–4%) extends from eastern Tibet to the region around the southeastern margin of Tibet and northern Burma in an approximate NS direction. On this map, a clear boundary approximately along lat-

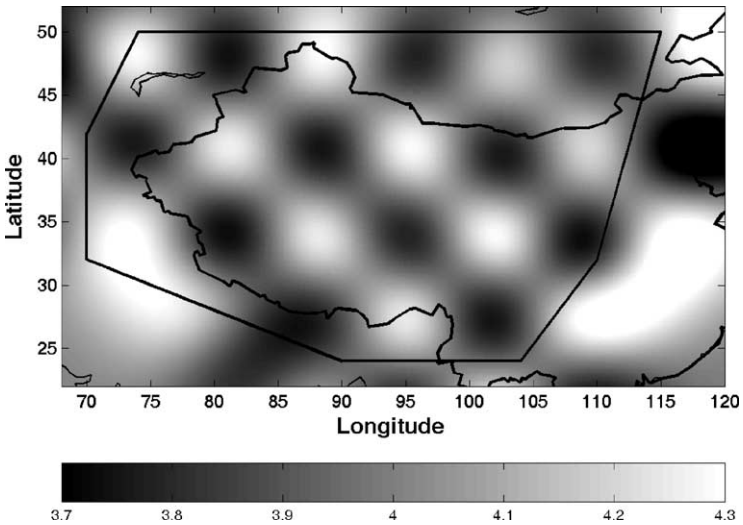

Fig. 5. $7^\circ \times 7^\circ$ Checkerboard tests of resolution. The bold black line on this map is the outermost margin of our reliable area. The results outside this margin are unreliable.

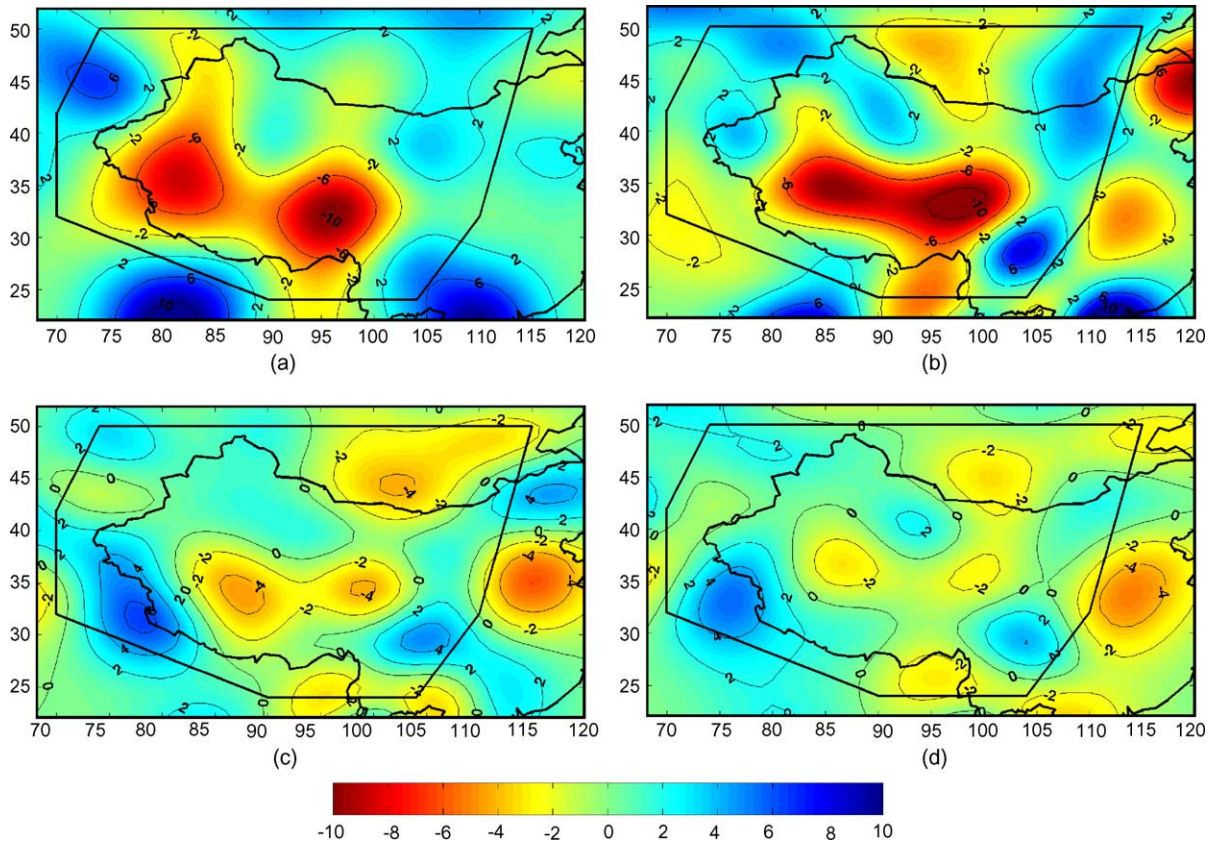

Fig. 6. Maps of Rayleigh wave phase velocities variation (in percentage with respect to WChina1D results) for: (a) 20 s, (b) 40 s, (c) 80 s, and (d) 120 s. The averaged phase velocity value is 3.361 km/s for 20 s, 3.760 km/s for 40 s, 4.017 km/s for 80 s, and 4.156 km/s for 120 s.

itude 105° (Zhu et al., 2002; Huang et al., 2003) divides continental China into west and east parts. The western part of China has a much thicker crust compared with the eastern part, especially in the Tibet plateau with the crust thickness about 70 km. Western Mongolia also shows a low-velocity anomaly (−2–4%) (Trampert and Woodhouse, 1995, 1996; Ekstrom et al., 1997; Curtis et al., 1998). The Sichuan basin shows very clear high-velocity anomaly (about +6%). A high-velocity anomaly also exists in the regions around the Junggar basin and Turpan depression, western Tianshan–Tarim, the northeastern Kazakhstan, eastern Mongolia and Inner Mongolia.

In the 80 s map (Fig. 6c), the main low-velocity anomaly in the Tibetan plateau (about −4%) shrinks to the Chang Thang terrane and northeastern Tibet; the magnitude of these anomalies is significantly less than the 40 s phase velocity map. The low-velocity anomaly still seems to cover a large part of the Tibetan plateau at the 80 s global map by Trampert and Woodhouse (1996). But in the 80 s regional map by Curtis et al. (1998), the low-velocity zone shrinks to a very short zone in the Chang Thang terrane, which is surrounded by a high-velocity anomaly and the eastern margin of Tibet shows a low-velocity anomaly; low-velocity zone still appears in northern Burma. A large part of Mongolia, mainly in central Mongolia, shows a low-velocity anomaly (−2–4%) and this low-velocity zone extends over a larger area in our 40 s map. In a similar way to the 40 s results, the Sichuan basin shows high-velocity anomaly (+4%). The central and northern Himalayan thrust and the Pamir region show a high-velocity anomaly of about +2–6%. These high-velocity features also appear in the maps of Trampert and Woodhouse (1995, 1996), Curtis et al. (1998), Ekstrom et al. (1997) and Griot and Montag-

ner (1998). At 120 s period (Fig. 6d), the low-velocity anomaly (+2%) still exists in the north Chang Thang terrane, northeastern Tibet, northern Burma and central Mongolia. The Sichuan basin and the central and northern Himalayan thrust still show high-velocity feature with slightly lower magnitude compared with 80 s map.

For the most part of our studied regions, the phase velocities of Rayleigh wave fundamental mode at lower periods (20 and 40 s) are much more sensitive to the *SV* structure in the crust while at higher periods (80 and 120 s) Rayleigh wave phase velocities are more sensitive to the upper mantle *SV* structure. From the phase velocity maps (Fig. 6), the velocity anomaly (in percentage) at lower periods (20 and 40 s) is much larger than the anomaly at higher periods (80 and 120 s); this clearly indicates that the lateral heterogeneity in the crust of our region of study is much larger than that in the upper mantle.

5. Discussion

This is the first time that inter-station method was used to perform Rayleigh wave phase velocity tomography in western China and its surrounding area. Because the inter-station method could very well suppress the errors in dispersion measurements, we are confident of our data quality after very careful comparison and selection with the help of image analysis technique and the corresponding GUI software. Although the number of the inter-station paths we used here is much less than that of pervious global and regional phase velocity studies (Trampert and Woodhouse, 1995, 1996; Ekstrom et al., 1997; Curtis et al., 1998), the lateral resolution in their studies vary from about 750 to 1000 km which is almost equal to or lower than the lateral resolution (about 7°) in our study. Griot and Montagner (1998) argued that their lateral resolution for Rayleigh waves structure was about 350 km, but the actual resolution in their study will gradually decrease as the period increases.

Here, we present some results of 1D dispersion data derived from the tomographic inversion for some critical points at the map (Fig. 7). Fig. 7a shows dispersion curves for five main points in Tibet. Seismic and geologic evidence shows that the India shield subducts northward beneath the south margin of Tibet and the Pamir; the Himalayan Mountains are the thrust and collision boundary. The dispersion curve for northwestern Himalayas region (latitude: 32°N; longitude: 76°E) is distinguished by its much higher phase velocity than any other part of the Tibetan plateau at intermediate and higher periods, which is consistent with the subduction of the cold and rigid Indian plate lithosphere beneath the Himalayan thrust. At 120 s, the Rayleigh wave phase velocity reaches about 4.4 km/s, about +5% higher than 4.2 km/s of PEMc (Fig. 4a). From Fig. 7a, the phase velocities for one typical point (latitude: 30°N; longitude: 97°E) in southeastern Tibet are very low at shorter and intermediate periods (about 15–50 s, compared with WChina1D), which probably implies a low *SV* wavespeed structure at the depth around the midlower crust and uppermost mantle in this region. Eastern Tibet is traditionally interpreted as being part of the broad accommodation zone (about 700 km wide), which has absorbed deformation induced by the indentation of India into Asia (Dewey et al., 1988; Yin and Harrison, 2000). Huang et al. (2003) pointed out that the sub-Moho low-velocity zone in Tibet extends eastward to about 102° and then turns southward along the eastern margin of Tibet and slightly deviates to west, until it connects the prominent low-velocity zone at the Burma–China border. This feature in our 40 s phase velocity map shows a good resemblance to the results by Huang et al. (2003).

At periods above 20 s (Fig. 7a), the phase velocities for the point (latitude: 35°N; longitude: 87°E) in the north Chang Thang terrane are lower than those for the point (latitude: 30°N; longitude: 90°E) in the central Lhasa block, which implies the average *SV* structure of the midlower crust and upper mantle of central Lhasa block is obviously higher than that of the north Chang Thang terrane. The two dispersion curves have great differences especially at intermediate periods (35–60 s) that are most sensitive to *SV* structure of the lower crust and uppermost mantle. In northern and central Tibet, especially around the north Chang Thang terrane, a clear low-velocity anomaly most probably in the lower crust and uppermost mantle is displayed in our results (Figs. 6 and 7a), similar to the regional tomographic results of Bourjot and Romanowicz (1992), Curtis et al. (1998) and Griot and Montagner (1998). This region was found to be an area of subrecent basaltic volcanism (Kidd, 1975; Gansser, 1980). Brandon and Romanowicz (1986) showed the Chang Thang terrane

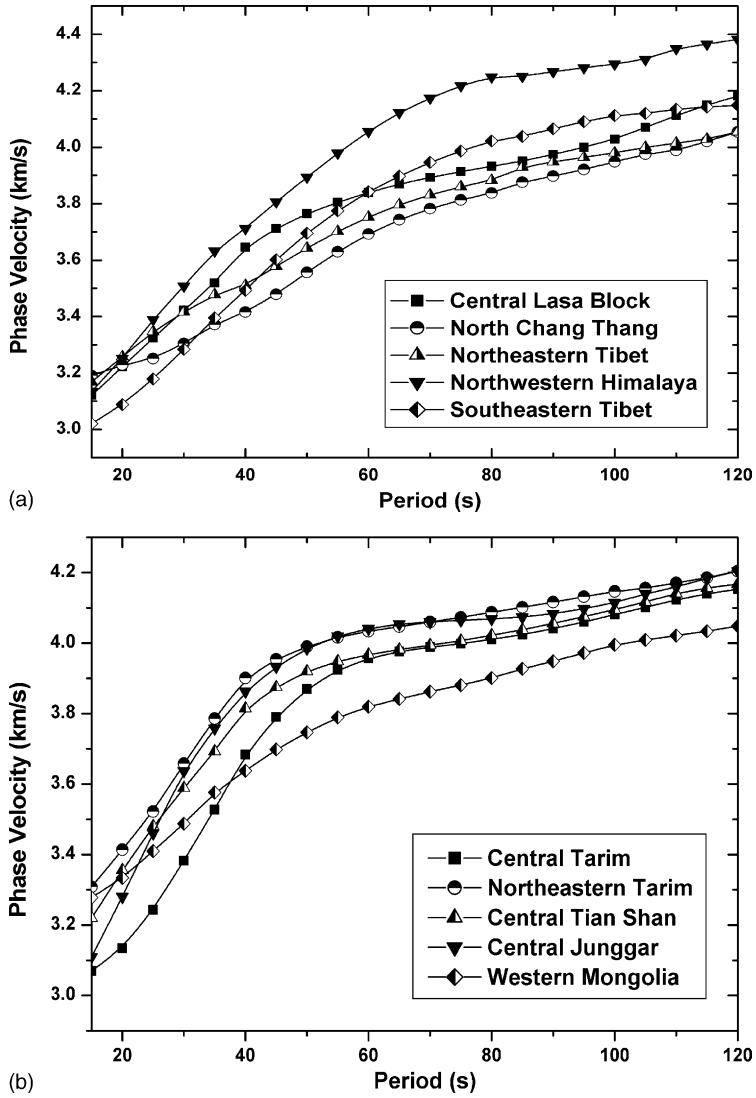

Fig. 7. Rayleigh wave phase velocities for some critical points in our studied area after tomographic inversion. (a) Central Lhasa block: 30°N, 90°E; north Chang Thang: 35°N, 87°E; northeastern Tibet: 36°N, 100°E; northwestern Himalayas: 32°N, 76°E; southeastern Tibet: 30°N, 97°E. (b) Central Tarim: 39°N, 82°E; northeastern Tarim: 41°N, 90°E; central Tian Shan: 42°N, 79°E; central Junggar: 46°N, 86°E; western Mongolia: 46°N, 98°E.

is inefficient for Sn waves transmission and lacks a high velocity lithospheric lid. Curtis and Woodhouse (1997) indicated that a widespread low-velocity mantle layer exists within the depth range 115–180 km beneath the central and northeast plateau. Huang et al. (2003) indicated that in the north of the Banggong-Nujiang suture and south of the Kunlun Mountains (approximately between 32° and 36°) the top part of the mantle shows abnormally low velocities. They also pointed out a prominent low-velocity zone existing in the middle crust of Qiang Thang terrance and Lhasa block. McNamara et al. (1994) and Owens and Zandt (1997) showed low S-velocity and high Poisson's ratio lie in the crust of the north Chang Thang terrane and Songpan-Ganzi fold system and indicated that the lower crust of central Tibet has partially melted. Magnetotelluric studies (Wei

et al., 2001) indicate that high-conductivity layer is at 30–40 km in northern Tibet and is mainly caused by the partial melting. And in central Chang Thang terrane the high-conductivity region extends to the upper mantle (at least 100 km depth from their results). Geochemical evidence (Molnar et al., 1993) of Plio-Pleistocene volcanic rocks derived from mantle is also consistent with the high conductivity, low velocity and high attenuation property in this region suggesting a localized upwelling within the asthenosphere (Brandon and Romanowicz, 1986; Molnar et al., 1993; Curtis et al., 1998; Wei et al., 2001) mainly caused by partial melting in the lower crust and uppermost mantle.

The dispersion curve of one typical point (latitude: 36°N; longitude: 100°E) in northeastern Tibet also shows a prominent low-velocity feature at periods between 40 and 70 s compared with the dispersion curve of the central Lhasa block (Fig. 7a). We also find that the dispersion curve of northeastern Tibet lies between that of central Lhasa block and that of the north Chang Thang terrane at periods from about 35 to 110 s. From our phase velocity maps (Fig. 6), northeastern Tibet shows apparent low-velocity anomaly at almost every period. Seismic evidence from receiver functions (Vergne et al., 2002) indicated that the northeastern Tibet shows unusually low Poisson's ratio and probably lacks a high velocity mafic lower crust (Rudnick and Fountain, 1995; Christiansen, 1996; Galve et al., 2002). The inversion result of Vergne et al. (2002) showed that in north Kunlun of northeastern Tibet the shear wave velocity of the lower crust is significantly lower than that of the middle crust; in their results a low-velocity (about 4.2 km/s) anomaly in the uppermost mantle (about 60–80 km) also exists. A shear wave velocity profile along longitude 100°E (Huang et al., 2003) also shows a low-velocity anomaly about 4.2 km/s in the uppermost mantle in a small region of northeastern Tibet, whereas in our study (Fig. 6) this low-velocity zone seems to be much broader than theirs.

The Tarim basin is regarded as a relatively rigid and stable Proterozoic platform surrounded by active fold belts and orogens. Figs. 6 and 7b show that the *SV* structure beneath Tarim varies with position. The phase velocities of northeastern Tarim (latitude: 41°N; longitude: 90°E) are obviously higher than those of central Tarim (latitude: 39°N; longitude: 82°E), especially below 60 s (Fig. 7b), implying a more rigid structure in the northeastern Tarim than in central Tarim. At 15 s, the phase velocities of the central Tarim and central Junggar (latitude: 46°N; longitude: 86°E) are very low (about 3.1 km/s), perhaps caused by the thick sediments in both basins (Laske and Masters, 1997). At periods higher than 25 s, the dispersion curve of northeastern Tarim is very similar to that of central Junggar. The phase velocities of central Tian Shan (latitude: 42°N; longitude: 79°E) are about 1–2% lower than those of northeastern Tarim for our studied periods and almost equal to those of central Tarim at periods above 60 s. From Fig. 7b, the phase velocities of western Mongolia (latitude: 46°N; longitude: 98°E) show prominent low-velocity feature at periods above 30 s. From our tomography results (Fig. 6), a large-scale low-velocity zone appears in western Mongolia at period 40 s, whereas at 20 and 40 s maps (Fig. 6a and b) a clear high-velocity anomaly appears in eastern Mongolia. At 80 and 120 s maps, the low velocity zone mainly lies in central Mongolia. The profiles of Huang et al. (2003) clearly indicate that the *SV* structure at the upper mantle is higher in eastern Mongolia than in western and central Mongolia with a very thick asthenosphere beneath. A large-scale asthenospheric upwelling beneath the Baikal rift has been widely supported by geophysical, geological and geochemical evidences (Windley and Allen, 1993; Gao et al., 1994; Petit et al., 1996; Ionov, 2002). The thick asthenosphere lying in western and central Mongolia may have a significant relationship with this large-scale asthenospheric upwelling beneath the Baikal rift.

Because the inter-station method can give phase velocity measurements with much higher quality than other methods, the limited 110 measurements in this paper can be used to evaluate some existing models for our studied region. Here, we chose the latest CUB global shear velocity model of the crust and upper mantle (Shapiro and Ritzwoller, 2002) because the CUB model is derived from a very large data set of fundamental mode surface wave group and phase velocities (Rayleigh group velocities, 16–200 s; Love group velocities, 16–150 s; Rayleigh and Love phase velocities, 40–150 s). The Rayleigh phase velocity maps predicted from CUB model are presented on a $2^\circ \times 2^\circ$ grid globally so we calculated the predicted arrive time t^i_{CUB} (i, path index) for each inter-station path at periods 40, 60, 80, and 100 s by bilinear interpolation. The observed arrival time for each inter-station path is t^i_{Obs}. We calculated the average relative error (ARErr), the average

positive error (APErr) and the average negative error (ANErr) in percentage by:

$$\mathrm{ARErr} = \frac{1}{N}\sum_{i}\frac{t^i_{\mathrm{CUB}} - t^i_{\mathrm{Obs}}}{t^i_{\mathrm{Obs}}} \times 100\% \quad (6)$$

$$\mathrm{APErr} = \frac{1}{N_P}\sum_{t^i_{\mathrm{CUB}} > t^i_{\mathrm{Obs}}}\frac{t^i_{\mathrm{CUB}} - t^i_{\mathrm{Obs}}}{t^i_{\mathrm{Obs}}} \times 100\% \quad (7)$$

$$\mathrm{ANErr} = \frac{1}{N_N}\sum_{t^i_{\mathrm{CUB}} < t^i_{\mathrm{Obs}}}\frac{t^i_{\mathrm{CUB}} - t^i_{\mathrm{Obs}}}{t^i_{\mathrm{Obs}}} \times 100\% \quad (8)$$

N is the total number of inter-station paths (in our study is 110); N_P is the total number of paths satisfying $t^i_{\mathrm{CUB}} > t^i_{\mathrm{Obs}}$ whereas N_N is the total number of paths satisfying $t^i_{\mathrm{CUB}} < t^i_{\mathrm{Obs}}$. In Section 2, we have mentioned that the phase velocity errors at periods above 35 s were not larger than 0.04 km/s (about 1%), so we consider here that the predicted phase velocity map at a certain period from the CUB model is consistent with our measurement along a inter-station path if at this period the relative error for this path is lower than 1%. Thus, we only need to pick the paths with the relative error $(t^i_{\mathrm{CUB}} - t^i_{\mathrm{Obs}})/t^i_{\mathrm{Obs}} \times 100\%$ higher than 1% at our interested periods. We separately counted the number N_{+1} of paths with relative error higher than 1% and the number $N_{-1}$of paths with relative error low than −1%. Table 1 shows our results, and Fig. 8 displays paths with relative error higher than 1% and relative error low than −1% in separate maps at periods 40 and 100 s. The width of the line used for inter-station path in Fig. 8 represents the magnitude of the relative error.

From Table 1, ARErr is only above 1% at period 40 s. At 40 s, APErr is about 0.5% higher than the absolute value of ANErr and N_{+1}/N is about 45%, implying the Rayleigh phase velocities predicted from CUB model for our studied region are somewhat high at 40 s. From Fig. 8a, the region with higher wavespeed of their 40 s map maybe covers a large part of western China and perhaps also includes western Mongolia. The average magnitude of discrepancy in western China maybe reaches +2% or more and in western Mongolia this value is about +1%. At 60 and 80 s, from Table 1, the Rayleigh phase velocities predicted from CUB model for this region are consistent with most of our measurements and only show slightly higher wavespeeds. At 100 s, from Table 1 and Fig. 8c, ARErr is slightly higher than that of 60 or 80 s. Although the absolute value of ANErr is about 0.1% higher than APErr, N_{+1} is twice larger than N_{-1}, which probably implies that the 100 s map for the studied region from CUB model is also a little fast and the region with higher wavespeeds (Fig. 8c) mainly lies in central and northern Tibet with magnitude about +1%. From the discussion above, the inconsistency between the predicted arrival time from CUB model and our measurements reaches a maximum at 40 s at which period Rayleigh phase velocity is mainly sensitive to the crustal thickness and the velocity structure around Moho depth in our studied area, whereas for global studies, the Rayleigh phase velocity at 40 s is mainly sensitive to the upper mantle shear velocity structure in the ocean area and some continental cratons which only have very thin crustal thickness. So at 40 s, the lateral variation is very prominent at global phase velocity maps. The construction of CUB model is based on a two-step inversion of surface waves. The first step is called surface wave tomography to estimate 2D dispersion maps and the second step is an inversion of the shear velocity structure of the crust and upper mantle from dispersion data on each geographical grid point. One possible reason that caused the overestimated of the Rayleigh phase velocity at 40 s in western China and western Mongolia from CUB model is due to the Gaussian smoothing condition that was applied to the model in the first tomography inversion step (Shapiro and Ritzwoller, 2002), which probably suppressed or mitigated the most prominent low-velocity anomaly in western China and neighboring western Mongolia in both phase velocity and group velocity maps, thereby causing the overestimated shear velocity around the Moho depth or an underestimated crustal thickness. Although other reasons maybe also caused these over-estimated results of CUB model, we suggest that the Gaussian smoothing condition in their tomography inversion is the main reason for the difference from our results.

Table 1
Evaluation of CUB model using our phase velocity measurements

	ARErr (%)	APErr (%)	ANErr (%)	N_{+1}	N_{-1}
40 s	1.27	1.37	−0.89	49	7
60 s	0.65	0.68	−0.61	17	7
80 s	0.64	0.65	−0.61	16	4
100 s	0.73	0.71	−0.83	21	9

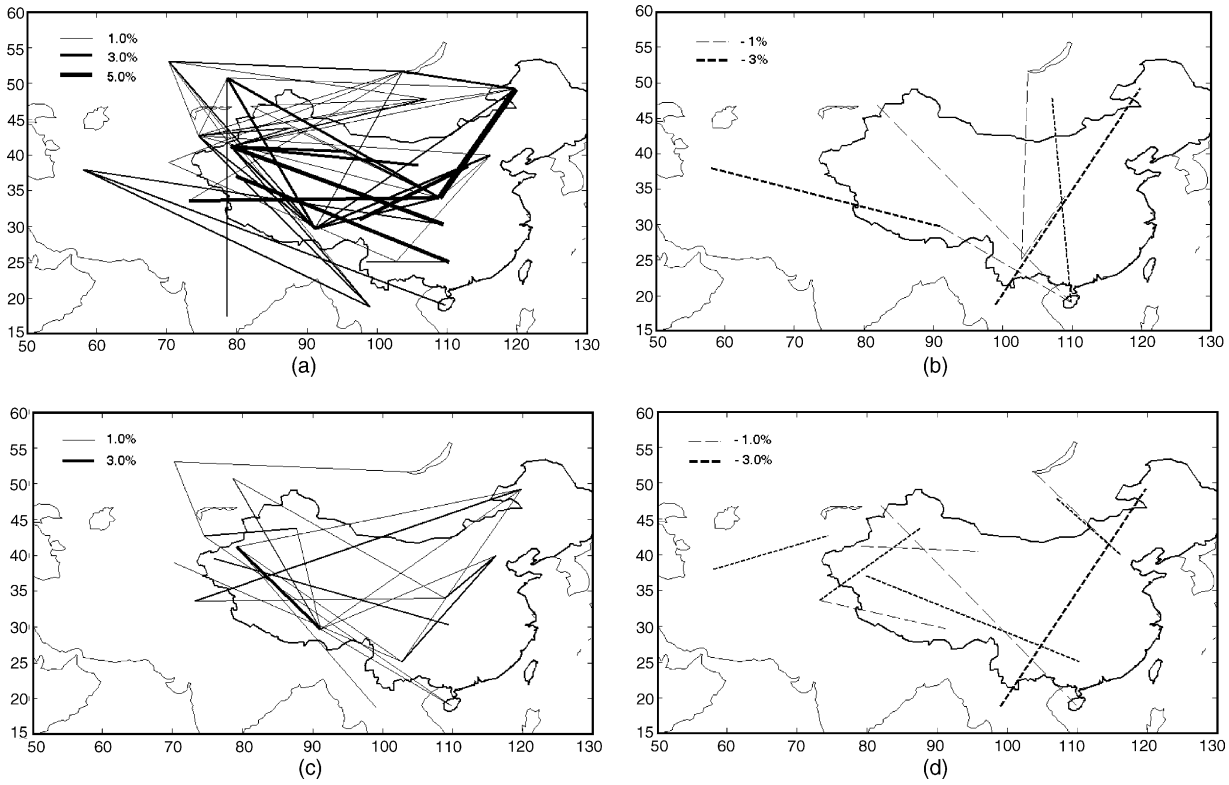

Fig. 8. Evaluation of CUB model using our phase velocity measurements. (a) Paths distribution on 40 s map; every path satisfying the relative error higher than 1%. (b) Paths distribution on 40 s map; every path satisfying the relative error lower than −1%. (c) Similar to (a), but for 100 s map. (d) Similar to (b), but for 100 s map. Here, the relative error is calculated by $(t^i_{\mathrm{CUB}} - t^i_{\mathrm{Obs}})/t^i_{\mathrm{Obs}} \times 100\%$ and the width of the path represents the magnitude of the relative error.

6. Conclusions

This is the first time that Rayleigh wave tomography is performed with inter-station method in western China and surrounding regions. Our results provide clear images of the lateral variation of the crust and upper mantle velocity structure in this area. Because the inter-station paths we used are well distributed in western China and adjacent regions, our 1D average Rayleigh wave phase velocity model WChina1D should best describe the features of Rayleigh wave dispersion in this geologically and tectonically complicated region. Phase velocity maps from 15 to 120 s were inverted using the ray approximation and the maps of 20, 40, 80, and 120 s were given in this paper. Checkerboard tests show the average lateral resolution in our interested area is about 7°. Our tomographic results confirm that the low-velocity anomaly in the Chang Thang terrane is probably caused by partial melting in the lower crust and uppermost mantle. Northeastern Tibet is another prominent low-velocity area clearly shown in our results. The low-velocity area around southeastern Tibet may be created by the southeastern migration of the low-velocity mass below the Tibetan plateau. The eastern Tarim shows relative higher velocity structure than that of central Tarim. A large-scale low-velocity anomaly is clearly seen in central and western Mongolia indicating the hot upper mantle and thick asthenosphere in this area. Our high quality measurements are also used to evaluate the global CUB shear velocity model of the crust and upper mantle. Rayleigh phase velocity map at 40 s predicted from CUB model shows an apparent discrepancy with our measurements in western China and western Mongolia, which implies a higher estimated phase velocity model (about +1–2%) in these regions, probably arising from

the Gaussian smoothing condition in their tomography inversion.

Acknowledgments

This research was supported by National Science Funds of China (49974008 and 40374010). We thank to IRIS for supplying major part of our data and also thank to the data center of CDSN for supplying the other part of our data. We are particularly grateful to Jean-Paul Montagner, Andrew Curtis and Jeannot Trampert for kindly supplying their tomographic results for comparison, Nikolai Shapiro for providing the predicted Rayleigh phase velocity data from CUB model, Dr. Sidao Ni of Caltech for his careful review of our manuscript and Anatoli Levshin for helpful referee reports.

References

Bloch, S., Hales, A.L., 1968. New techniques for the determination of surface wave phase velocities. Bull. Seismol. Soc. Am. 58, 1021–1034.

Bourjot, L., Romanowicz, B., 1992. Crust and upper mantle tomography in Tibet using surface waves. Geophys. Res. Lett. 19, 881–884.

Brandon, C., Romanowicz, B., 1986. A "no-lid" zone in the central Chang-Thang platform of Tibet: evidence from pure path velocity measurements of long-period Rayleigh waves. J. Geophys. Res. 91, 6547–6564.

Brisbourne, A., Stuart, G., 1998. Shear-wave velocity structure beneath North Island, New Zealand, from Rayleigh-wave interstation phase velocities. Geophys. J. Int. 133, 175–184.

Brune, J.N., Nafe, J.E., Oliver, J.E., 1960. A simplified method for the analysis and synthesis of dispersed wave trains. J. Geophys. Res. 65, 287–304.

Calcagnile, G., 1991. Deep-structure of fennoscandia from fundamental and higher mode dispersion of Rayleigh-waves. Tectonophysics 195, 139–149.

Cara, M., Leveque, J.J., 1987. Waveform inversion using secondary observables. Geophys. Res. Lett. 14, 1046–1049.

Christiansen, N.I., 1996. Poisson's ratio and crustal seismology. J. Geophys. Res. 102, 3139–3156.

Curtis, A., Woodhouse, J.H., 1997. Crust and upper mantle shear velocity structure beneath the Tibetan plateau and surrounding regions from the interevent surface wave phase velocity inversion. J. Geophys. Res. 102, 11789–11813.

Curtis, A., Trampert, J., Snieder, R., 1998. Eurasian fundamental mode surface wave phase velocities and their relationship with tectonic structures. J. Geophys. Res. 103, 26919–26947.

Dewey, J.F., Shackelton, R.M., Chang, C., Sun, Y., 1988. The tectonic evolution of the Tibetan plateau. Philos. Trans. R. Soc. Lond. A 327, 379–413.

Dziewonski, A.M., Anderson, D.L., 1981. Preliminary reference Earth model. Phys. Earth Planet. Interact. 125, 297–356.

Dziewonski, A.M., Bloch, S., Landisman, M., 1969. A technique for the analysis of transient seismic signals. Bull. Seismol. Soc. Am. 59, 427–444.

Dziewonski, A.M., Hales, A.L., Lapwood, 1975. Parametrically simple Earth models consistent with geophysical data. Phys. Earth Planet. Interact. 10, 12–48.

Ekstrom, G., Tromp, J., Larson, E.W.F., 1997. Measurements and global models of surface wave propagation. J. Geophys. Res. 102, 8137–8157.

Feng, C.C., Teng, T., 1983. Three-dimensional crust and upper mantle structure of the Eurasian continent. J. Geophys. Res. 88, 2261–2272.

Feng, R., Zhu, J.S., Ding, Y.Y., Chen, G.Y., He, Z.Q., Yang, S.B., Zhou, H.N., Sun, K.Z., 1983. Crustal structure in China from surface waves. Chin. Geophys. Am. Geophys. Union 2, 273–289.

Galve, A., Hirn, A., Jiang, M., Gallart, et al., 2002. Mode of raising northeastern Tibet probed by explosion seismology. Earth Planet. Sci. Lett. 203, 35–43.

Gansser, A., 1980. The signification of the Himalayan suture zone. Tectonophysics 62, 37–52.

Gao, S., Davis, P.M., Liu, H., Slack, P.D., Zorin, Y.A., et al., 1994. Seismic anisotropy and mantle flow beneath the Baikal rift-zone. Nature 371, 149–151.

Griot, D.A., Montagner, J.P., 1998. Phase velocity structure from Rayleigh and Love waves in Tibet and its neighboring regions. J. Geophys. Res. 103, 21215–21232.

Huang, Z., Su, W., Peng, Y., et al., 2003. Rayleigh wave tomography of China and adjacent regions. J. Geophys. Res. 103 (B2), ESE 4-1–ESE 4-14.

Ionov, D., 2002. Mantle structure and rifting processes in the Baikal–Mongolia region: geophysical data and evidence from xenoliths in volcanic rocks. Tectonophysics 351, 41–60.

Jobert, N., Journet, B., Hirn, A., Zhong, S.K., 1985. Deep structure of southern Tibet inferred from the dispersion of Rayleigh waves through a long-period seismic network. Nature 313, 386–388.

Kidd, W.S.F., 1975. Wildspread late Neogene and quaternary calc-alkaline vulcanism on the Tibetan plateau. EOS Trans. AGU 56, 453.

Knopoff, L., Muller, S., Pilant, W.L., 1966. Structure of the crust and upper mantle in the Alps from the phase velocity of Rayleigh waves. Bull. Seismol. Soc. Am. 56, 1009–1044.

Landisman, M., Dziewonski, A., Sato, Y., 1969. Recent improvements in the analysis of surface wave observations. Geophys. J. R. Astron. Soc. 17, 369–403.

Laske, G., Masters, G., 1997. A global digital map of sediment thickness. Eos Trans. AGU 78, F483 (Abstract).

Lévêque, J.J., Rivera, L., Wittlinger, G., 1993. On the use of the checkerboard test to assess the resolution of tomographic inversions. Geophys. J. Int. 115, 313–318.

McNamara, D.E., Owens, T.J., Silver, J.L., Wu, F.T., 1994. Shear wave anisotropy beneath the Tibetan plateau. J. Geophys. Res. 99, 13655–13665.

Molnar, P., Tapponnier, P., 1978. Active tectonics of Tibet. J. Geophys. Res. 83, 5361–5375.

Molnar, P., England, P., Martinod, J., 1993. Mantle dynamics, uplift of the Tibetan plateau, and the Indian monsoon. Rev. Geophys. 31, 357–396.

Nolet, G., 1990. Partitioned waveform inversion and two-dimensional structure under the network of autonomously recording seismographs. J. Geophys. Res. 95, 8499–8512.

Owens, T.J., Zandt, G., 1997. Implications of crustal property variations for models of Tibetan plateau evolution. Nature 387, 37–43.

Petit, C., Deverchere, J., Houdry, F., et al., 1996. Present-day stress field changes along the Baikal rift and tectonic implications. Tectonics 15, 1171–1191.

Ritzwoller, M., Levshin, A., 1998. Eurasian surface wave tomography: group velocities. J. Geophys. Res. 103, 4839–4878.

Ritzwoller, M., Levshin, A., Ratnikova, L., Egorkin, A., 1998. Intermediate-period group velocity maps across Central Asia, western China and parts of the Middle East. Geophys. J. Int. 134, 315–328.

Ritzwoller, M., Shapiro, N., Barmin, M., Levshin, A., 2002. Global surface wave diffraction tomography. J. Geophys. Res. 107 (B12), 2335, doi:10.1029/2002JB001777.

Romanowicz, B., 1982. Constraints on the structure of the Tibet plateau from pure-path phase velocities of Love and Rayleigh waves. J. Geophys. Res. 87, 6865–6883.

Rudnick, R.L., Fountain, D.M., 1995. Nature and composition of the continental crust: a lower crustal perspective. Rev. Geophys. 33, 267–309.

Sato, Y., 1958. Attenuation, dispersion, and the wave guide of the G wave. Bull. Seismol. Soc. Am. 48, 231–251.

Shapiro, N., Ritzwoller, M., 2002. Monte-Carlo inversion for a global shear-velocity model of the crust and upper mantle. Geophys. J. Int. 151, 88–105.

Snoke, J., James, D., 1997. Lithospheric structure of the Chaco and Parana Basins of South America from surface-wave inversion. J. Geophys. Res. 102, 2939–2951.

Spetzler, J., Trampert, J., Snieder, R., 2002. The effect of scattering in surface wave tomography. Geophys. J. Int. 149, 755–767.

Tarantola, A., Nercessian, A., 1984. Three-dimensional inversion with blocks. Geophys. J. R. Astron. Soc. 76, 299–306.

Trampert, J., Woodhouse, J., 1995. Global phase velocity maps of Love and Rayleigh waves between 40 and 150 seconds. Geophys. J. Int. 122, 675–690.

Trampert, J., Woodhouse, J., 1996. High resolution global phase velocity distributions. Geophys. Res. Lett. 23, 21–24.

Trampert, J., Woodhouse, J., 2001. Assessment of global phase velocity models. Geophys. J. Int. 144, 165–174.

Vergne, J., Wittlinger, G., Hui, Q., Tapponnier, P., Popinet, G., et al., 2002. Seismic evidence for stepwise thickening of the crust across the NE Tibetan plateau. Earth Planet. Sci. Lett. 203, 25–33.

Wei, W.B., Unsworth, M., Jones, A., Brook, J., Tan, H.D., et al., 2001. Detection of widespread fluid in the Tibetan crust by magnetotelluric studies. Science 292, 716–718.

Windley, B.F., Allen, M.B., 1993. Mongolian plateau—evidence for a late Cenozoic mantle plume under Central Asia. Geology 21, 293–298.

Wu, F.T., Levshin, A., 1994. Surface-wave group velocity tomography of East Asia. Phys. Earth Planet. Interact. 94, 59–77.

Xu, G.M., Li, G.P., Wang, S.E., Chen, H., Zhou, H.S., 2000. The 3-D structure of shear waves in the crust and mantle of east continental China inverted by Rayleigh wave data. Chinese J. Geophys. 43, 366–376 (in Chinese).

Yao, H.J., Xu, G.M., Xiao, X., Zhu, L.B., 2004. A quick tracing method based on image analysis technique for the determination of dual stations phase velocities dispersion curve of surface wave. Seismol. Geomagn. Observ. Res. 25 (1), 1–8 (in Chinese).

Yin, A., Harrison, T.M., 2000. Geologic evolution of the Himalayan–Tibetan orogen. Annu. Rev. Earth Planet. Sci. 28, 211–280.

Yoshizawa, K., Kennett, B.L.N., 2002a. Non-linear waveform inversion for surface waves with a neighborhood algorithm—application to multimode dispersion measurements. Geophys. J. Int. 149, 118–133.

Yoshizawa, K., Kennett, B.L.N., 2002b. Determination of the influence zone for surface wave paths. Geophys. J. Int. 149, 441–454.

Zhu, L.B., Xu, Q., Chen, X.F., 2002. Group velocity of Rayleigh wave in Chinese continent and its adjacent seas. Chin. J. Geophys. 45, 475–482 (in Chinese).